Research Square

Preprints are preliminary reports that have not undergone peer review.
They should not be considered conclusive, used to inform clinical practice,
or referenced by the media as validated information.

High-Order Harmonic Generation in Zinc Oxide Driven by a 1.5-Cycle Mid-Infrared Vortex Beam

Rajaram Shrestha
ELI ALPS, The Extreme Light Infrastructure ERIC
Bikash Kumar Das
Friedrich Schiller University Jena
Debobrata Rajak
ELI ALPS, The Extreme Light Infrastructure ERIC
Eric Cormier
ELI ALPS, The Extreme Light Infrastructure ERIC
Stephan Fritzsche
Friedrich Schiller University Jena
Wenlong Gao
Eastern Institute of Technology, Ningbo
Balint Kiss
ELI ALPS, The Extreme Light Infrastructure ERIC
Camilo Granados
cagrabu@eitech.edu.cn

Eastern Institute of Technology, Ningbo

Article

Keywords:

Posted Date: November 10th, 2026

DOI: https://doi.org/10.21203/rs.3.rs-11452577/v1

License: This work is licensed under a Creative Commons Attribution 4.0 International License.
Read Full License

Additional Declarations: No competing interests reported.

High-Order Harmonic Generation in Zinc Oxide Driven by a 1.5-Cycle Mid-Infrared Vortex Beam

Rajaram Shrestha[1], Bikash Kumar Das[2], Debobrata Rajak[1], Eric Cormier[1,3], Stephan Fritzsche[2,4,5], Wenlong Gao[6], Bálint Kiss[1,*], and Camilo Granados[6,*]

[1]ELI ALPS, The Extreme Light Infrastructure ERIC, Wolfgang Sandner u. 3., 6728 Szeged, Hungary.
[2]Theoretisch-Physikalisches Institut, Friedrich-Schiller-Universität Jena, Max-Wien-Platz 1, Fröbelstieg 3, D-07743 Jena, Germany
[3]Laboratoire Photonique Numérique et Nanosciences (LP2N), UMR 5298, CNRS-IOGS-Université Bordeaux, 33400 Talence, France
[4]Helmholtz-Institut Jena, D-07743 Jena, Germany
[5]GSI Helmholtzzentrum für Schwerionenforschung GmbH, Planckstr. 1, D-64291 Darmstadt, Germany
[6]Eastern Institute of Technology, Ningbo 315200, China
[*]Balint.Kiss@eli-alps.hu
[*]cagrabu@eitech.edu.cn

ABSTRACT

The interaction of twisted light with matter opens up new regimes of light–matter physics. Here, we demonstrate the generation of few-cycle (1.5-cycle) mid-infrared vortex beams with a pulse duration of ≈ 16 fs, characterized in both the temporal and spectral domains. By compensating the temporal dispersion introduced by the spiral phase plate, we preserve the characteristic doughnut-shaped spatial structure of the vortex beam while achieving near-transform-limited pulse durations. We use these ultrashort vortex beams to drive high-order harmonic generation in zinc oxide and investigate whether the orbital angular momentum is preserved in the generated harmonics. We show that harmonic vortices with a well-defined topological charge can still be produced despite the large spectral bandwidth of the driving field, following the linear OAM upscaling rule $\ell_q = q\ell_0$. However, when the inversion symmetry of the crystal is broken, the combination of the few-cycle driving field and the reduced spectral separation between even- and odd-order harmonics leads to OAM mode overlap and contamination. These results establish practical limits on the generation of pure harmonic vortices with few-cycle driving fields and demonstrate that the interplay between the pulse duration and the crystal symmetry can be exploited to engineer the spatial structure and topological charge of high-harmonic radiation, including the generation of fractional vortex beams.

Introduction

Traditionally, the generation of short pulses was restricted to beams with well-defined Gaussian intensity distribution since these are relatively easy to produce and manipulate in the laboratory[1–4]. However, with the advent of liquid-crystal spatial light modulators and various other optical elements for twisting the light beam's phase, it has become possible to induce nonlinear, non-perturbative effects in atoms and solids with helical beams[5–7]. Coherent light beams carrying orbital angular momentum (OAM), also known as vortex beams or twisted light, are pivotal to understanding how physical systems interact with, and can be controlled via, the spatial phase distribution of a beam's wavefront[8–10].

Significant theoretical and experimental advances have demonstrated that helical dichroism controls the absorption of twisted light by atoms, molecules, and solids[11–13]. Furthermore, twisted light can coherently imprint OAM on a propagating electron wave, an effect known as the dichroic photoelectric effect[8]. In another application, researchers demonstrated that high-order harmonic generation (HHG) driven by twisted light enables the coherent transfer of OAM from the driving field to the generated harmonics, following the linear OAM up-scaling rule $\ell_q = q\ell_0$[6,14,15]. Here, ℓ_0 is the topological charge (TC) of the driving field, q is the harmonic order, and ℓ_q is the TC carried by the harmonic field. This rule is limited to interactions that respect the dipole approximation. Moreover, twisted light-driven HHG in atomic targets has revealed a novel property of light – the self-torque of light – wherein the OAM of the generated extreme ultraviolet radiation varies dynamically over time[16]. More importantly, the rich landscape of spatial structures and their distinct properties makes OAM beams a perfect candidate to extend light–matter interaction processes into the femtosecond and attosecond regimes.

By displacing the dark core of a vortex beam, researchers extended its interaction with matter beyond the dipole limit and to demonstrate effects such as dichroism-dependent matter response[11,17]. In Ref.[17], beyond-dipole corrections were found to typically induce symmetry breaking in HHG, thereby leading to the emergence of even-order harmonics in the spectra.

Furthermore, the generation of few-cycle femtosecond vortex beams with high peak power was theoretically proposed via their self-compression in thin plates[18]. Yet, within this large number of applications, it is still not clear how the interaction of few- to single-cycle vortex beams can modify this OAM selection rule, since the resulting harmonic vortices always have a larger bandwidth than the driving field[19]. How the extra broadband spectral components affect the OAM selection rule, what TC they carry, and how they interact with the target system still remain open questions. Nevertheless, the harmonic generation process is highly intensity-dependent, which results in a filtering of the beam's sidebands, possibly clearing out the small OAM sidebands around the central wavelength.

Here, we take a step toward understanding the interaction of few-cycle light with matter by generating and characterizing few-cycle vortex beams. We apply those beams to investigate the HHG process in solid-state materials and demonstrate that it results in two different scenarios: (i) well-defined harmonics for a c-cut zinc oxide (ZnO) crystal, and (ii) mode contamination for an a-cut ZnO crystal. Our work establishes limits on the generation of harmonic vortices with a well-defined TC and opens the door to studying how different controllable properties of the fundamental beam in combination with distinct crystal configurations can be used to engineer the OAM carried by harmonic vortex beams.

Experimental measurements

The experiment was performed at the ELI-ALPS facility using a mid-infrared optical parametric chirped-pulse amplifier (MIR OPCPA; BLACK STARZZ, Fastlite)[20]. A schematic representation of the experimental setup, comprising the post-compression scheme and the harmonic generation stage, is shown in Fig. 1 (a) and Fig. 1 (b), respectively. Operating at a repetition rate of 100 kHz, the system delivers 100 μJ pulses (10 W average power) centered at 3.2 μm, with an initial pulse duration of 45 fs[20]. The driver output features a power and pulse-to-pulse energy stability below 1% RMS, and low CEP noise ($<$ 150 mrad). Furthermore, pointing fluctuations were actively compensated using an Aligna beam stabilization system (TEM Messtechnik).

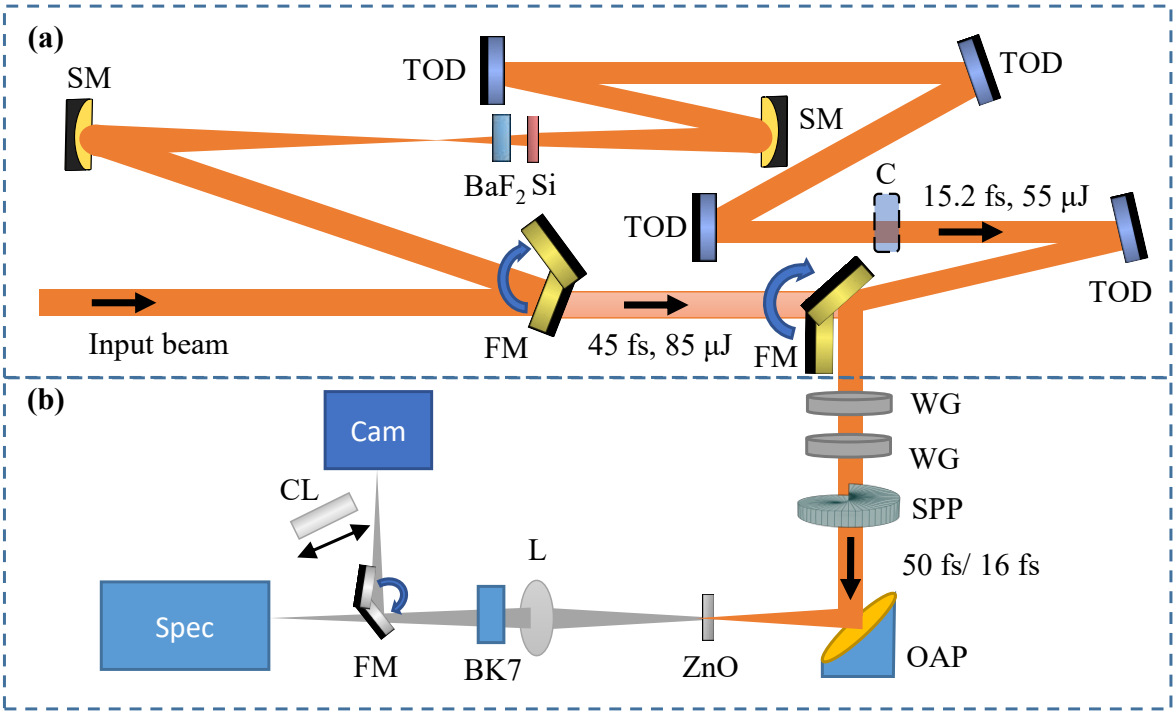


Figure 1. Schematic representation of the experimental setup. (a) Nonlinear post-compression scheme for the MIR pulses utilizing bulk-based spectral broadening in barium fluoride (BaF_2) and silicon (Si) plates, followed by third-order dispersion (TOD) mirrors and bulk compressing windows (C) for compression management. Flip mirrors (FMs) enable selection between the uncompressed and post-compressed MIR pulses. SM: spherical mirror. (b) HHG and vortex beam diagnostic setup. The vortex beam is focused onto a ZnO crystal using an off-axis parabolic mirror (OAP). The 3.2 μm fundamental driver is suppressed by a BK7 substrate, and the generated harmonic signals are directed via a focusing lens (L) and a FM to either a UV-Vis spectrometer (Spec) or a beam-profiling camera (Cam) for characterization of the vortex beam profile. A cylindrical lens (CL) is used to measure the TC. WG: wire-grid polarizer; SPP: spiral phase plate.

The generation of the few-cycle vortex beam is described as follows. We first compressed the Gaussian output of the

mid-infrared laser and then modified the experimental setup to accommodate the spectral dispersion induced by the spiral phase plate (SPP) and two 3-mm-thick BaF_2 wire-grid polarizers (WGs). A pair of WGs was used to provide fine power control while preserving the linear *s*-polarization, whereas the SPP was used for generating vortex beams. The compressed Gaussian driver beam was generated via the nonlinear post-compression technique, as described in Ref.[21]. In short, a fraction (85 μJ) of the total pulse energy was focused into an in-air confocal arrangement using two unprotected gold-coated spherical mirrors (SMs, $f = 500$ mm). Self-phase modulation (SPM) was induced via a sequence of uncoated 5 mm BaF_2 and anti-reflection (AR)-coated 1 mm Si substrates positioned downstream of the focal waist to prevent spatial breakdown and catastrophic self-focusing. Post-broadening temporal re-compression was achieved using three bounces of custom-made, third-order dispersion (TOD) mirrors (OPTOMAN) paired with bulk compressors (C) consisting of 5 mm CaF_2 and 5 mm BaF_2 windows, yielding 15.2 fs pulses with 55 μJ energy.

Table 1. Dispersion parameters of the optical materials and TOD mirrors used for generating the few-cycle vortex beam at 3.2 μm.

Materials	GVD (fs^2)	TOD (fs^3)
Fused Silica	-780 per mm	5703 per mm
BaF_2	-63 per mm	390 per mm
CaF_2	-130 per mm	745 per mm
Si	488 per mm	868 per mm
TOD Mirror	137 per bounce	-3600 per bounce

To compress the vortex beam for the HHG experiments, we modified the re-compression stage, following the description in Ref.[21]. In terms of optical material, the SPP introduces an additional group velocity dispersion (GVD) that corresponds exactly to 1 mm thick SK-1300 fused silica (FS) window, together with additional TOD. To compensate for both, we added one more TOD mirror and removed the 5 mm CaF_2 window. The compressor now comprises a pair of 3 mm-thick BaF_2 wire-grides (WGs) and a 1 mm FS window. Furthermore, the WGs introduce the dispersion previously provided by the 5 mm BaF_2 window[21]. The new compressor was designed to compensate the material dispersion introduced by the SPP and the WGs, which results in a pulse duration of $\approx$ 16 fs. As a result, we could safely remove the primary compressor (C) without compromising the vortex beam pulse duration, since the required dispersion to shorten the driving pulse is now introduced by the SPP and the WGs. Consequently, the vortex beam compressor contains four TOD reflections, two WGs, and the SPP. Based on the GVD and TOD parameters noted in Table 1, this dispersion-balanced, SPP-containing configuration, yields an estimated pulse duration of 16 fs. Conversely, dispersion from the two WGs and the SPP broadened the uncompressed reference beam to a duration of $\approx$ 50 fs. To evaluate the reference beam under comparable conditions, we inserted dispersion-equivalent optics (matching the SPP) into its path.

Depending on the configuration enabled by the flip-mirrors (FMs), either the long (50 fs, 85 μJ) or the short (16 fs, 55 μJ) structured light beam was directed towards the HHG line, as presented in Fig. 1 (b). We then focused the driver vortex pulse onto a 50 μm-thick ZnO crystal with a-cut (1120) and c-cut (0001) orientations, using an off-axis parabolic mirror (OAP, $f = 150$ mm). The generated harmonic vortices were collected by a lens (L, $f = 150$ mm) after suppressing the 3.2μm fundamental beam with a BK7 substrate. A FM routed the signal either to an Avantes spectrometer (Spec) or a Basler camera (Cam) for vortex beam's spectral or spatial profiling. Here, we inserted a cylindrical lens (CL, $f = 500$ mm) to measure the TC of vortices via astigmatic mode transformation[22,23]. The CL typically transforms a vortex beam into a tilted Hermite-Gauss-lobed intensity pattern, where the number of minima between the maximum-intensity lobes directly relates to the TC carried by the vortex beam.

Results and discussion

The nonlinear post-compression dynamics and characterization of the MIR vortex beams are summarized in Fig. 2 and Fig. 3. The initial laser spectrum (blue trace, central wavelength $\lambda_0 \approx 3.2\,\mu$m) spans between 2850 nm and 3650 nm, supporting a Fourier-transform-limited (FTL) pulse duration of $\tau_{\mathrm{FTL}} = 44.6$ fs [Fig. 2]. Following nonlinear propagation, the output spectrum expands dramatically, spanning more than an octave i.e., from 2000 nm to more than 4000 nm (red trace). This spectral broadening reduces the FTL pulse duration to $\tau_{\mathrm{FTL}} = 14.7$ fs, creating the spectral bandwidth necessary to support few-cycle pulse formation. Additionally, to verify the experimental vortex-beam compression and phase linearity, we used the tunneling ionization with a perturbation for the time-domain observation of an electric field (TIPTOE) technique [Fig. 3][24]. The dispersive effect of the SPP was simulated using a 1 mm thick SK-1300 FS window, since the TIPTOE technique does not work for the vortex beam due to the doughnut-shaped spatial intensity distribution. The retrieved temporal electric field of the vortex driver $E(t)$ [Fig. 3 (a)] confirms the compression from a broad, $\approx$ 4-cycle waveform ($E(t)_{\mathrm{Long}}$, gray shading) to a

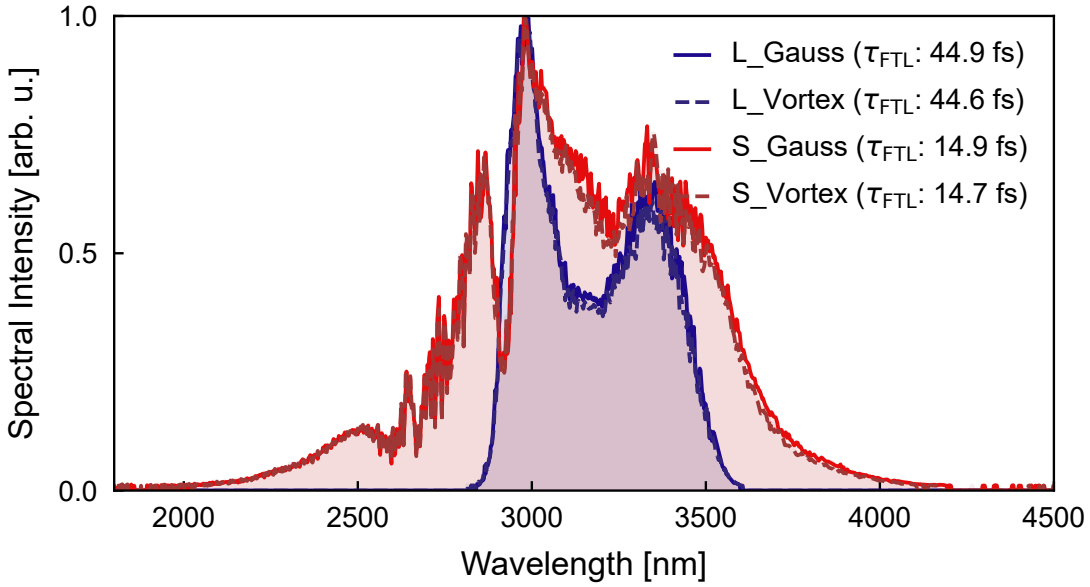


Figure 2. Measured spectral broadening following post-compression. Comparison of the initial spectrum (Long, blue line) and the broadened spectrum after nonlinear propagation (Short, red line). For the Gaussian beam, the calculated transform-limited pulse duration (τ_{FTL}) decreases from 44.9 fs to 14.9 fs. Similarly, for the vortex beam, τ_{FTL} decreases from 44.6 fs to 14.7 fs. Here and in all plots, "arb. u." stands for arbitrary unit.

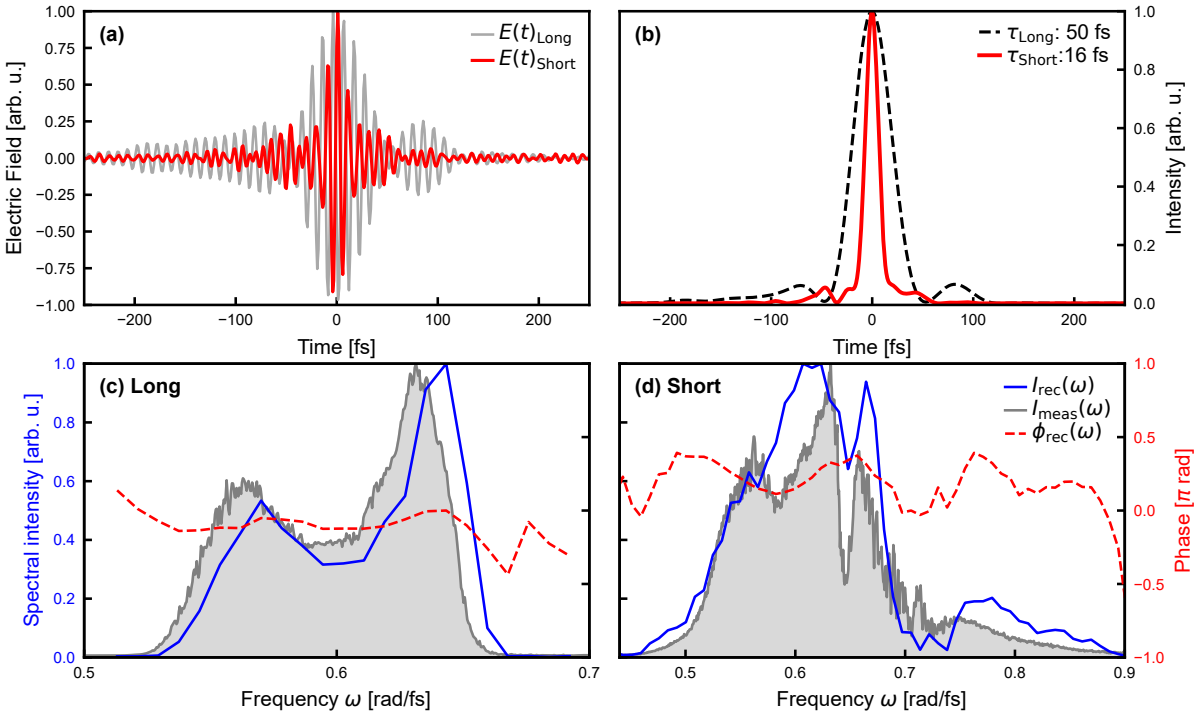


Figure 3. Temporal and spectral characterization of the long and short MIR pulses via TIPTOE. (a) Reconstructed electric fields $E(t)$ with a fixed, cosine absolute CEP, for the Long (solid gray) and Short (solid red) pulses. (b) Corresponding temporal intensity profiles showing compression from $\tau_{Long} = 50$ fs (black dashed) down to $\tau_{Short} = 16$ fs (solid red). (c,d) TIPTOE retrieval results for the (c) Long and (d) Short pulses, comparing the spectrum measured by the spectrometer, $I_{meas}(\omega)$ (gray shaded), with the retrieved spectral intensity $I_{rec}(\omega)$ (solid blue) and spectral phase $\phi_{rec}(\omega)$ (red dashed, right axis). The spectra are normalized to their respective maximum intensities.

localized, sub-two-cycle structure ($E(t)_{\mathrm{Short}}$, solid red trace). Correspondingly, the temporal intensity profiles of the vortex beam [Fig. 3 (b)] demonstrate pulse shortening from an initial pulse duration of $\tau_{\mathrm{Long}} = 50$ fs to $\tau_{\mathrm{Short}} = 16$ fs. Moreover, the fidelity of the temporal reconstruction is further supported by spectral-domain benchmarking [Fig. 3(c)–(d)]. A comparison between the independently measured spectrometer data $I_{\mathrm{meas}}(\omega)$ (gray filled region) and the TIPTOE-retrieved spectral intensity $I_{\mathrm{rec}}(\omega)$ (solid blue curve) shows strong agreement for the short vortex beam across the entire frequency range (0.43-0.92 rad/fs). Notably, following dispersion compensation [Fig. 3(d)], the retrieved spectral phase $\phi_{\mathrm{rec}}(\omega)$ (dashed red line) remains almost flat ($\phi_{\mathrm{rec}}(\omega) \approx 0$ rad) across the main spectral body. The negligible deviation between the measured pulse duration (16 fs) and the calculated transform limit (14.7 fs) confirms the generation of near-transform-limited vortex beams.

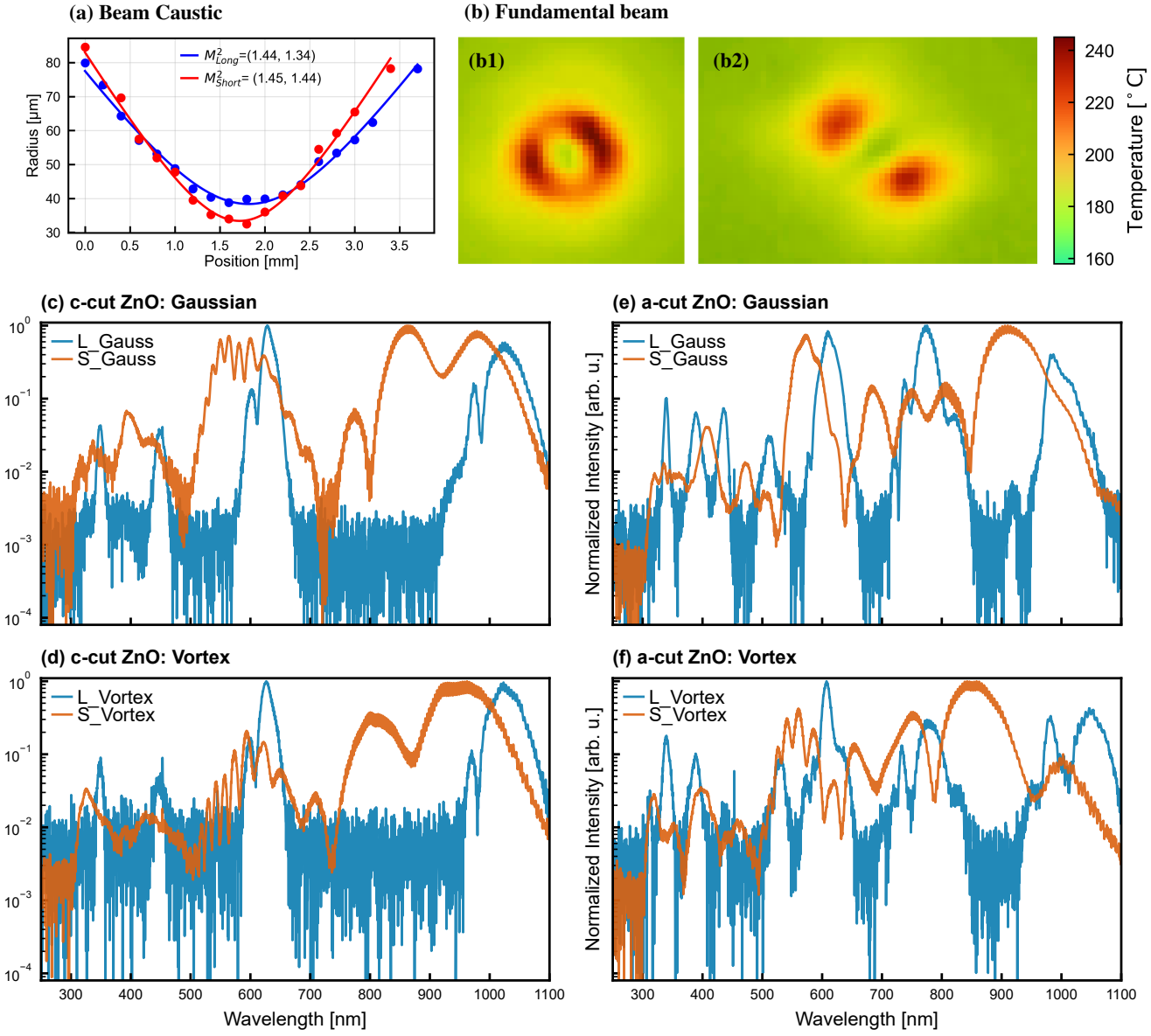


Figure 4. Generation of high-order harmonics driven by ultrashort Gaussian and vortex MIR pulses in ZnO. (a) Beam caustic measurement for long and short Gaussian beam. (b) Comprises of: (b1) transverse intensity distribution of the driving MIR vortex beam and (b2) its TC measurement using a CL. The color bar indicates temperature in °C (160–240 °C), representing the beam's thermal profile captured by an infrared camera. HHG spectra recorded from a 50 μm-thick ZnO crystal are shown for the c-cut orientation under (c) Gaussian and (d) vortex beam driving, and for the a-cut orientation under (e) Gaussian and (f) vortex beam driving. Spectra generated by long 50 fs pulses (L, blue) are compared with short 16 fs pulses (S, orange). All spectra are normalized to their respective maximum intensities.

Now, we use the ≈ 1.5-cycle vortex beam to drive HHG in the ZnO crystal. The two chosen orientations of ZnO crystals generate different harmonic orders: the c-cut ZnO produces only odd-order harmonics, whereas the a-cut ZnO produces both even- and odd-order harmonic vortices. For the long driving pulse (4-cycle), it has already been demonstrated that it is possible to generate harmonic vortices with a well-defined TC[25]. However, it is not clear whether the short vortex pulse will create OAM mode contamination in the harmonic spectra, particularly when the combination of the few-cycle pulse and the a-cut ZnO crystal is used. To answer this question, we characterized, both spatially and spectrally, the vortex beam in the far-field. As shown in the beam caustic measurement [Fig. 4 (a)], the beam propagation factor M^2 on both x- and y-axis remains close to the diffraction limit for both configurations, with values of M^2 = (1.44, 1.34) for the long pulse and M^2 = (1.45, 1.44) for the short pulse. An example of the resulting measurements together with the produced harmonic spectra for both crystal cuts is presented in Fig. 4 (c)–(f). Spatial beam profiles of the fundamental 3.2 μm driver [Fig. 4 (b)] were captured using a bolometer-based thermal camera. The driver pulse carries a well-defined integer TC ($\ell_0 = 1$), with no multimode nature detectable within the resolution of our experimental technique, even for the few-cycle pulse duration [Fig. 4 (b1)–(b2)]. The assignment of a well-defined integer TC of 1 to the driver pulse is corroborated by two key observations from Fig. 4 (b1)–(b2): first, the transverse intensity distribution of the driver, shown in panel (b1), displays a continuous ring structure, and second, the tilted Hermite-Gauss-lobed pattern in panel (b2) exhibits a single intensity minimum between its two bright lobes. Additionally, we adopt the convention that the tilted Hermite-Gauss-lobed pattern oriented at approximately 135° corresponds to a positive TC, and we apply the same sign convention when determining the TC of the generated harmonic vortices. For both long Gaussian and vortex pulses in the c-cut ZnO crystal, the resulting harmonic spectra show no mode overlap [Fig. 4 (c) and (d)].

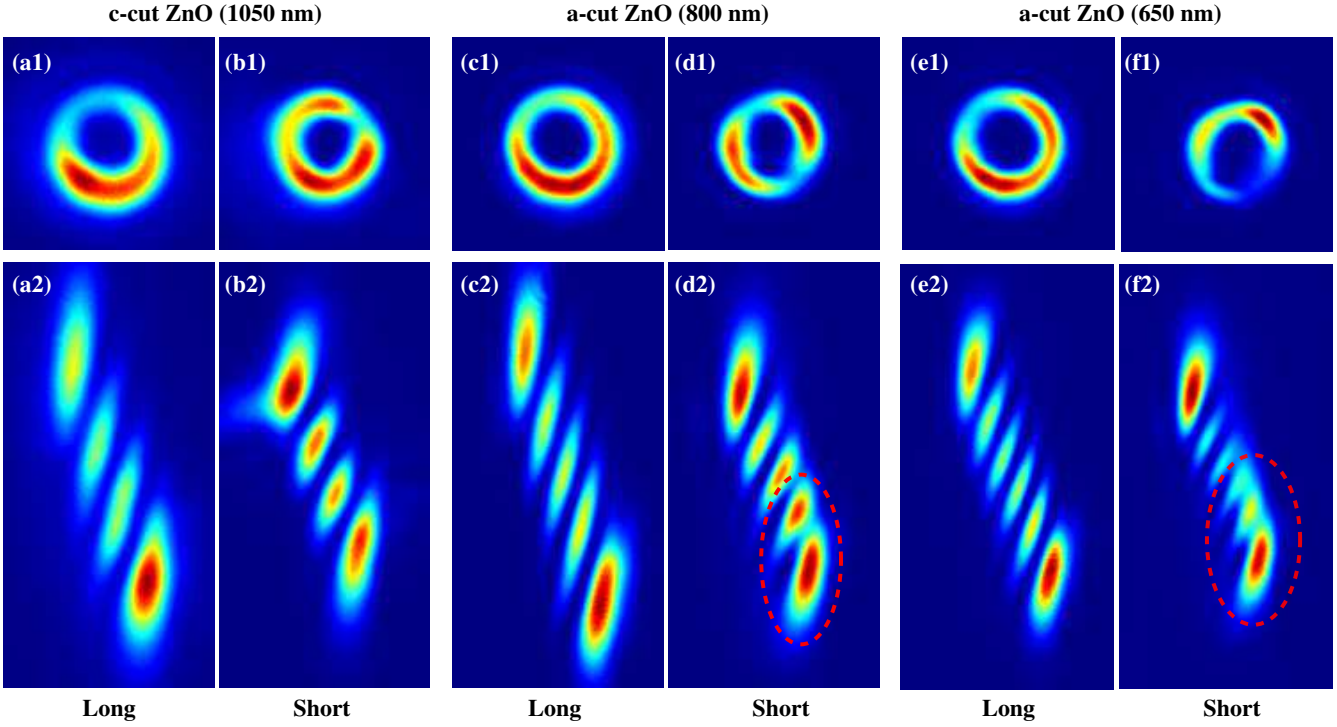


Figure 5. Transverse intensity distributions of the harmonic vortices and their corresponding TC measurements. (a1)–(f1) Harmonic vortex beam profiles and (a2)–(f2) corresponding TC measurements for the uncompressed (Long) and post-compressed (Short) pulses. The third harmonic vortex at 1050 nm was generated in a c-cut ZnO crystal [(a1), (b1)], while the fourth and fifth harmonic vortices at 800 nm [(c1), (d1)] and 650 nm [(e1), (f1)] were generated in an a-cut ZnO crystal respectively. All intensities are normalized to unity. Mode contamination in the compressed pulse cases is highlighted by dashed red ovals in (d2) and (f2).

Interestingly, even for the short pulse, the harmonics generated in the c-cut ZnO do not overlap, and harmonics at the central wavelength can be generated with a well-defined TC. This is clearly visible from Fig. 5 (a1)–(a2) and Fig. 5 (b1)–(b2), where we observe continuous intensity rings, well-defined vortex cores, and clearly-resolved Hermite-Gauss intensity lobes. This is also true for the harmonic vortex generation in an a-cut ZnO crystal driven by a long pulse [Fig. 5 (c1)–(c2), and (e1)–(e2)]. Notably, in case of short Gaussian and vortex pulses driving HHG in the c-cut ZnO crystal, we observe that the intensity of the 5th harmonic is strongly modulated [see the oscillations around 650 nm in Fig. 4 (c) and (d)]. These oscillations primarily arise

from the interference between the 5th harmonic radiation generated at the front and rear surfaces of the ZnO crystal. However, this spectral interference disappears approximately below 500 nm, possibly due to absorption of the light produced at the front surface of the crystal. So, below 500 nm, only the harmonic radiations generated at the rear surface of the crystal reach the detector. Such a behavior was also reported in Ref.[26], where a short Gaussian pulse drove the HHG process in a c-cut ZnO crystal.

This scenario is different for the a-cut ZnO crystal driven by the few-cycle driver. The interaction generates a broader harmonic spectrum whose wavelengths overlap even in the low-harmonic-order spectral region, due to the generation of even-order harmonics [Fig. 4 (e) and (f)]. This is particularly evident in the spectral region between 400 and 800 nm, where for the compressed pulse, the multiple peaks indicate an interference between the harmonic orders. This, in turn, leads to the overlapping of OAM modes, which is visible in harmonic vortices and the TC measurements as a broken vortex, existence of multiple dark cores, and a poorly-defined tilted Hermite-Gauss intensity pattern [Fig. 5 (d1)–(d2) and (f1)–(f2)]. The broken vortex distribution and the overlap of the bottom lobe with its immediately adjacent lobe are clear evidence of the multi-mode OAM nature of the harmonic vortex. Furthermore, from the transverse intensity distributions shown in Fig. 5 (a1)–(f1), it is evident that there exists a single dark core in panels (a1), (b1), (c1), and (e1), whereas multiple dark cores can be seen in panels (d1) and (f1). This also highlights the composite vortex nature of the harmonic beam in (d1) and (f1). Note that for the other TC measurements, the minima are well defined. Furthermore, from the TC measurements, it is not possible to infer the TC of the fourth and fifth harmonics in the case of a short-pulse driver, since the two bottom lobes overlap. In contrast, for the third harmonic generated in the c-cut ZnO crystal, the TC is $\ell_q = 3$, which strictly follows the linear OAM scaling law $\ell_q = q\ell_0$.

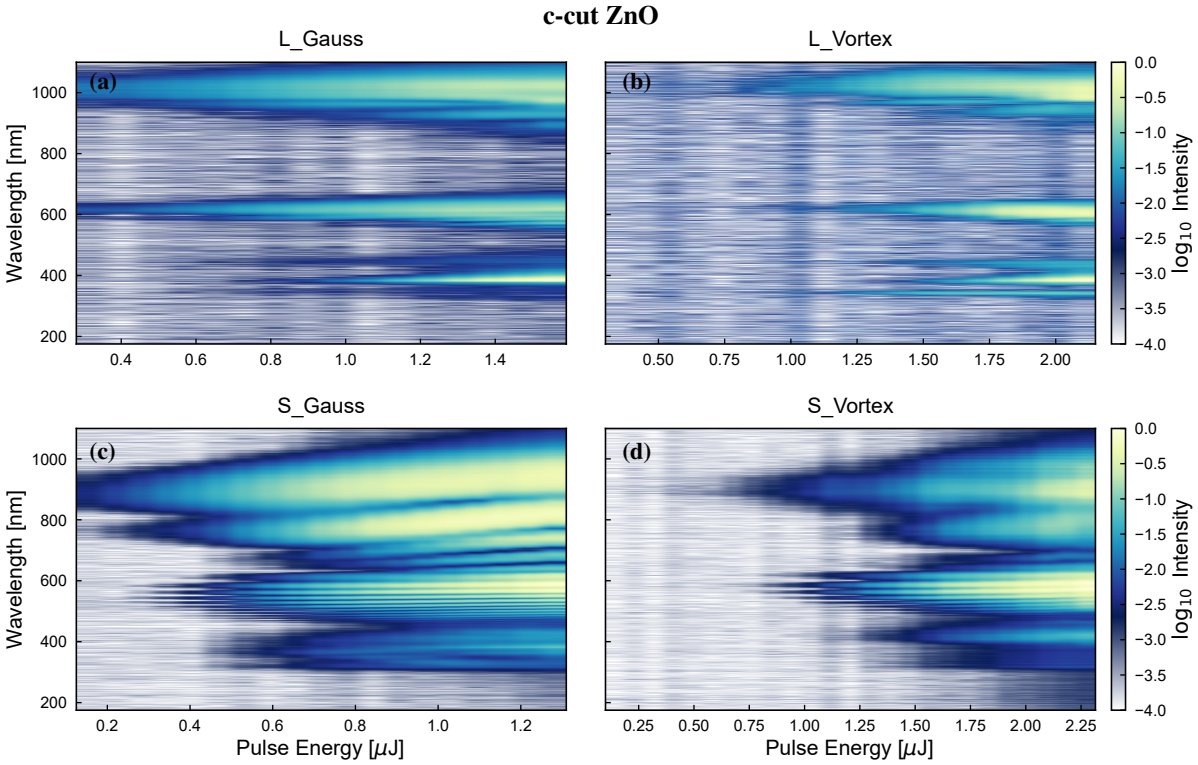


Figure 6. Power scan comparison. High-harmonic generation power scans in a c-cut 50 μm thick ZnO crystal under long-pulse and short-pulse regimes and for the Gaussian and vortex beams. In panels (a) and (b), we show the resulting power scan from the Gaussian and vortex beams in the long-pulse regime. The corresponding results for the short-pulse regime are presented in the panels (c) and (d). The different scans reveal the same trend for both the Gaussian and vortex beams. However, since the vortex beam has low power after passing through the optics required to generate it, harmonic generation begins at higher powers.

In addition, the power scans for both 50 μm thick c-cut and a-cut ZnO crystals, detailed across long-pulse and short-pulse regimes for both Gaussian and vortex beams, reveal distinct harmonic generation behaviors and threshold dynamics. For the c-cut ZnO crystal [Fig. 6], the power scans in panels (a) through (d) demonstrate consistent trends between the Gaussian and vortex beams, though harmonic generation initiates at higher pulse energies for the vortex beams due to power loss after the generation optics (SPP). Similarly, the a-cut ZnO [Fig. 7] exhibits higher initiation thresholds for vortex beams compared to

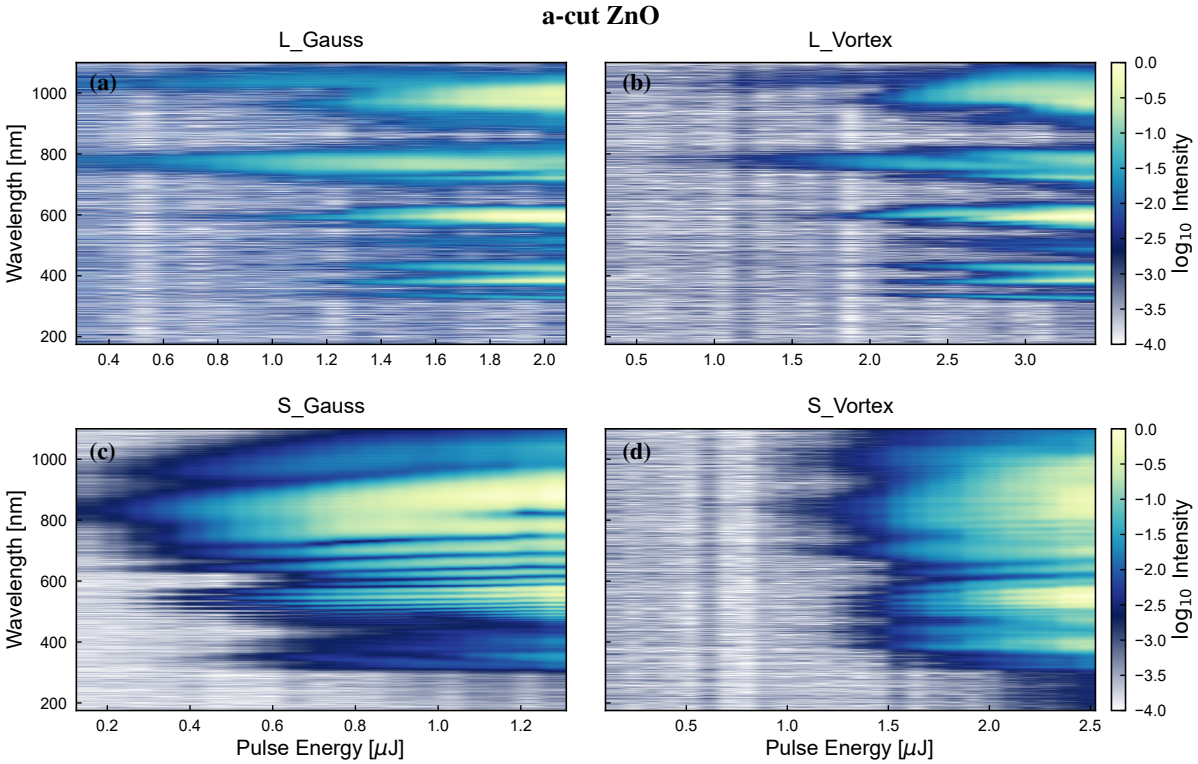


Figure 7. Power scan comparison. High-harmonic generation power scans in an a-cut 50 μm thick ZnO crystal under long-pulse and short-pulse regimes. In panel (a) and (b), we show the resulting power scan from the Gaussian and vortex beams in the long-pulse regime. The corresponding results for the short-pulse regime are presented in the panels (c) and (d). In contrast to the c-cut case, there is clear overlap between the harmonics in the power scan. Also, as observed in the previous case, harmonic generation occurs at higher powers for the vortex beam compared with the Gaussian beam.

Gaussian beams. However, unlike the c-cut crystal, the a-cut ZnO crystal power scans show a distinct and clear overlapping between the harmonics.

Across both orientations, short-pulse regimes [panels (c) and (d)] display more pronounced spectral broadening and high-harmonic signatures at lower pulse energies compared to their long-pulse counterparts [panels (a) and (b)]. For the long-pulse regime [50 fs, pulse energy $E_p = 2$ μJ, spot size $w_0 = 20$ μm], the calculated peak intensity reaches 3.1 TW/cm^2, which successfully drives HHG while remaining safely below the optical damage threshold of ZnO. In contrast, the theoretical calculation for the same pulse energy yields a lower peak intensity of 1.14 TW/cm^2, necessitating higher pulse energy to reach the required intensity threshold. To compensate for this, the calculated average power for the vortex beam was increased to $E_p = 3.5$ μJ, yielding a peak intensity of 2 TW/cm^2. Following a similar parametric analysis, the peak intensities for the short-pulse configuration [16 fs, $w_0 = 18$ μm] were evaluated for both Gaussian and vortex spatial modes. Specifically, the Gaussian beam achieves a calculated peak intensity of 6.6 TW/cm^2 (at $E_p = 1.2$ μJ), whereas the vortex beam attains a calculated peak intensity of 5.1 TW/cm^2 (at $E_p = 2.5$ μJ).

These results are important for two reasons: (i) the generation of few-cycle harmonic vortices with a well-defined TC via solid-state HHG is possible (up to the experimental sensitivity of the measuring technique), and for the spectral regions investigated here. In particular, when the HHG process is induced in materials that do not break inversion symmetry, that is, materials producing harmonic vortices with large spectral spacing between them. (ii) The more pronounced OAM mode overlap, resulting from the combination of an inversion-symmetry-broken crystal and the short pulse, can be exploited to engineer the TC of the resulting harmonic radiation, in particular for the generation of fractional vortex beams[27].

Conclusions

In conclusion, we have demonstrated the generation of few-cycle (1.5-cycle), mid-infrared vortex beams with a temporal duration of $\approx$ 16 fs. By compensating the dispersion introduced by the SPP, we preserve the spatial structure of the vortex beam while achieving near-transform-limited pulse durations, enabling the application of ultrashort vortex pulses to solid-state HHG.

Using ZnO crystals with different crystallographic orientations, we have investigated how the combination of the driving-pulse duration and crystal symmetry affects the OAM content of the generated harmonic radiation.

Our results show that few-cycle driving does not, by itself, prevent the generation of harmonic vortices with a well-defined TC. In c-cut ZnO, the harmonic vortices remain spatially well defined (up to our experimental sensitivity) even for the 1.5-cycle driving pulse, and the measured third harmonic follows the linear OAM upscaling rule $\ell_q = q\ell_0$. This demonstrates that the OAM structure of the driving field can survive the large spectral bandwidth associated with few-cycle pulses, most probably due to the nonlinearity of the process. In contrast, for the inversion-symmetry-broken a-cut ZnO, the simultaneous generation of even- and odd-order harmonics reduces the spectral separation between neighboring harmonic orders. For the few-cycle driver, the resulting spectral overlap produces interference between harmonic modes with different OAM content, leading to a measurable degradation of the vortex structure and TC measurement.

These observations establish practical limits on the OAM purity that can be achieved with short vortex pulses in solid-state HHG and show that the OAM content of the harmonic radiation is governed not only by the spatial structure of the driving field but also by the spectral structure of the generated harmonics. At the same time, the mode overlap observed in the inversion-symmetry-broken crystal should not be regarded solely as a limitation. The increased overlap between neighboring harmonic orders provides a mechanism for coherently combining OAM modes and thereby modifying the TC of the resulting radiation. This effect offers a route toward engineering harmonic vortex beams beyond the conventional integer OAM up-scaling rule, including the generation of fractional vortex beams.

More broadly, our results establish few-cycle vortex-driven HHG as a platform for investigating the interplay between temporal confinement, crystal symmetry, and spatial phase in nonlinear light–matter interactions. The ability to control the spectral and spatial mode content of the generated harmonics could enable the development of tailored vortex radiation at shorter wavelengths and provides a pathway toward studying light–matter interactions driven by non-integer-charge vortex beams, particularly in the XUV spectral region.

Acknowledgments

The ELI ALPS project (GINOP-2.3.6-15-2015-00001) is supported by the European Union and co-financed by the European Regional Development Fund. W. Gao acknowledges financial support from the National Natural Science Foundation of China (Grant number: 12474309). C.G. and B.K.D. acknowledge the support of the Extreme Light Infrastructure ERIC (ELI-ERIC) through the program “ELI Call for Users".

Author contributions statement

R.S., D.R., C.G., and B.K.D. made the experimental work. C.G., R.S., B.K.D., B.K., D.R., and E.C. conceptualized the idea. C.G., B.K., and W.G. prepared the materials for the experiments. R.S., C.G., and B.K.D. wrote the manuscript. C.G. and B.K. supervised the project. All authors reviewed and corrected the manuscript.

Conflict of Interest Statement

The authors declare no conflict of interest.

References

1. L’Huillier, A. Nobel lecture: The route to attosecond pulses. *Rev. Mod. Phys.* **96**, 030503, DOI: 10.1103/RevModPhys.96.030503 (2024).

2. Agostini, P. Nobel lecture: Genesis and applications of attosecond pulse trains. *Rev. Mod. Phys.* **96**, 030501, DOI: 10.1103/RevModPhys.96.030501 (2024).

3. Krausz, F. Nobel lecture: Sub-atomic motions. *Rev. Mod. Phys.* **96**, 030502, DOI: 10.1103/RevModPhys.96.030502 (2024).

4. Ghimire, S. & Reis, D. A. A tutorial on high-order harmonic generation in atoms, molecules, and condensed matter. *APL Photonics* **11**, 021102, DOI: 10.1063/5.0302159 (2026).

5. Zürch, M., Kern, C., Hansinger, P., Dreischuh, A. & Spielmann, C. Strong-field physics with singular light beams. *Nat. Phys.* **8**, 743–746, DOI: 10.1038/nphys2397 (2012).

6. Gariepy, G. *et al.* Creating high-harmonic beams with controlled orbital angular momentum. *Phys. Rev. Lett.* **113**, 153901, DOI: 10.1103/PhysRevLett.113.153901 (2014).

7. Das, B. K., Granados, C. & Ciappina, M. Optical vortices: revolutionizing the field of linear and nonlinear optics. *Adv. Physics: X* **11**, 2608076, DOI: 10.1080/23746149.2025.2608076 (2026).

8. De Ninno, G. *et al.* Photoelectric effect with a twist. *Nat. Photonics* **14**, 554–558, DOI: 10.1038/s41566-020-0669-y (2020).

9. Jhajj, N. *et al.* Spatiotemporal optical vortices. *Phys. Rev. X* **6**, 031037, DOI: 10.1103/PhysRevX.6.031037 (2016).

10. Lloyd, S. M., Babiker, M., Thirunavukkarasu, G. & Yuan, J. Electron vortices: Beams with orbital angular momentum. *Rev. Mod. Phys.* **89**, 035004, DOI: 10.1103/RevModPhys.89.035004 (2017).

11. Bégin, J.-L., Karimi, E., Corkum, P., Brabec, T. & Bhardwaj, R. Orbital angular momentum control of strong-field ionization in atoms and molecules. *Nat. Commun.* **16**, 2467, DOI: 10.1038/s41467-025-57618-8 (2025).

12. Bégin, J.-L. *et al.* Nonlinear helical dichroism in chiral and achiral molecules. *Nat. Photonics* **17**, 82–88, DOI: 10.1038/s41566-022-01100-0 (2023).

13. Jain, A. *et al.* Intrinsic dichroism in amorphous and crystalline solids with helical light. *Nat. Commun.* **15**, 1350, DOI: 10.1038/s41467-024-45735-9 (2024).

14. Hernández-García, C., Picón, A., San Román, J. & Plaja, L. Attosecond extreme ultraviolet vortices from high-order harmonic generation. *Phys. Rev. Lett.* **111**, 083602, DOI: 10.1103/PhysRevLett.111.083602 (2013).

15. Gauthier, D. *et al.* Orbital angular momentum from semiconductor high-order harmonics. *Opt. Lett.* **44**, 546–549, DOI: 10.1364/OL.44.000546 (2019).

16. Rego, L. *et al.* Generation of extreme-ultraviolet beams with time-varying orbital angular momentum. *Science* **364**, eaaw9486, DOI: 10.1126/science.aaw9486 (2019).

17. Albar, E. I., Kosheleva, V. P., Appel, H., Rubio, A. & Bonafé, F. P. High-order harmonic generation with orbital angular momentum beams: Beyond-dipole corrections. *Phys. Rev. A* **112**, 063109, DOI: 10.1103/c1yg-2svv (2025).

18. Xu, L., Li, D., Chang, J., Xi, T. & Hao, Z. Few-cycle vortex beam generated from self-compression of midinfrared femtosecond vortices in thin plates. *Phys. Rev. A* **106**, 053516, DOI: 10.1103/PhysRevA.106.053516 (2022).

19. Wu, S. *et al.* Analysis of extreme-ultraviolet vortex high-order harmonics generated by few-cycle laguerre-gaussian beams carrying orbital angular momentum. *Phys. Rev. A* **112**, 053103, DOI: 10.1103/b9bc-gw49 (2025).

20. Thiré, N. *et al.* Highly stable, 15 w, few-cycle, 65 mrad cep-noise mid-ir opcpa for statistical physics. *Opt. Express* **26**, 26907–26915, DOI: 10.1364/OE.26.026907 (2018).

21. Shrestha, R. *et al.* Single-cycle mid-infrared pulses with 30 μj at 100 khz via post-compression in solid-state media. *Opt. Lett.* **51**, 3184–3187, DOI: 10.1364/OL.599976 (2026).

22. Beijersbergen, M., Allen, L., van der Veen, H. & Woerdman, J. Astigmatic laser mode converters and transfer of orbital angular momentum. *Opt. Commun.* **96**, 123–132, DOI: 10.1016/0030-4018(93)90535-D (1993).

23. Padgett, M. J. & Allen, L. Orbital angular momentum exchange in cylindrical-lens mode converters. *J. Opt. B: Quantum Semiclassical Opt.* **4**, S17, DOI: 10.1088/1464-4266/4/2/362 (2002).

24. Cho, W., Shin, J.-u. & Kim, K. T. Reconstruction algorithm for tunneling ionization with a perturbation for the time-domain observation of an electric-field. *Sci. Reports* **11**, DOI: 10.1038/s41598-021-92454-y (2021).

25. Rajak, D. *et al.* Twisting harmonics: Transfer of orbital angular momentum in solid-state high-harmonic generation. *arXiv:2601.12743v1 [physics.optics]* DOI: 10.48550/arXiv.2601.12743 (2025).

26. Hollinger, R. *et al.* Carrier-envelope-phase measurement of few-cycle mid-infrared laser pulses using high harmonic generation in zno. *Opt. Express* **28**, 7314–7322, DOI: 10.1364/OE.383484 (2020).

27. Zhang, H. *et al.* Review on fractional vortex beam. *Nanophotonics* **11**, 241–273, DOI: doi:10.1515/nanoph-2021-0616 (2022).